ACS APPLIED MATERIALS & INTERFACES

www.acsami.org

Research Article

Atomic-Scale Behavior of Radiation-Resistant ZnO under High-Energy Electron Bombardment

Francisco Lagunas,* Shi Li, Zachary D. Hood, and Jessica C. Jones*

Cite This: https://doi.org/10.1021/acsami.5c04571

Read Online

ACCESS | Metrics & More | Article Recommendations | Supporting Information

ABSTRACT: Understanding the atomic structure and defect characteristics of ZnO thin films is crucial for optimizing their electronic properties and performance in advanced applications. Here, we investigate the atomic structure and defect characteristics of atomic layer deposition (ALD)-grown ZnO thin films by using aberration-corrected scanning transmission electron microscopy (STEM). Atomic-resolution imaging identifies prevalent stacking faults, dipole disorder, and various grain boundary types, which are believed to influence the electronic properties of ZnO. Additionally, real-time electron beam exposure experiments demonstrate structural transformations, including crystal growth and surface rearrangements. These findings provide insights into the growth mechanisms of ALD ZnO under high-energy electron irradiation conditions, an important finding for the use of polycrystalline ZnO wide bandgap semiconductors in space-like conditions. Our results underscore the capability of STEM in directly visualizing and quantifying atomic-scale defects and beam-induced transformations in radiation-resistant ZnO.

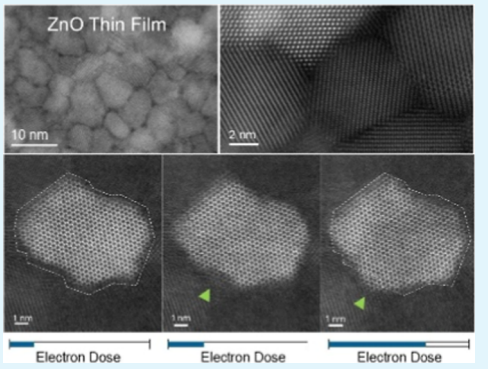

KEYWORDS: *scanning transmission electron microscopy (STEM), electron−sample interactions, wide bandgap semiconductors, zinc oxide, density functional theory (DFT), atomic defects*

INTRODUCTION

Zinc oxide (ZnO) is a semiconductor with applications in optoelectronics, sensors, and catalysis.[1] A combination of unique electronic and optical properties, including high exciton binding energy (60 MeV) and a wide band gap (3.37 eV), has made it a promising material for next-generation devices.[1−3] One area of particular interest is its use in microelectronics for space environments, where ZnO thin films outperform traditional silicon or GaAs semiconductors due to their high radiation hardness.[4,5]

Radiation resistance is critical for materials exposed to high-energy environments, as radiation can displace atoms from the crystalline lattice, forming vacancies or defect clusters that alter material properties.[6] In microelectronics, ionizing radiation can also induce single-event upsets (SEUs), where deposited energy flips a bit in a digital circuit, leading to data corruption or malfunctions.[7] The resilience of ZnO has been attributed to its ionic bonding and the predominance of spherically symmetric σ-orbitals, which may reduce the formation of radiation-induced defect states compared to covalently bonded semiconductors with highly directional sp-hybrid orbitals. However, its radiation response is also influenced by its wide band gap, defect tolerance, and self-healing properties.[8,9] Nevertheless, experimental evidence suggests additional mechanisms contribute to the behavior of ZnO under high-energy irradiation.[8−11] Notably, electron bombardment has been shown to enhance ZnO's UV emission, alter grain size and morphology, and improve its sensitivity in H_2 sensing applications.[12−14]

In this study, we use aberration-corrected scanning transmission electron microscopy (STEM) to probe the atomic structure of atomic layer deposition (ALD)-grown ZnO thin films. ALD offers precise control over film thickness and composition, making it a widely used technique for fabricating high-quality ZnO films.[15] However, the structural and defect characteristics of ALD-grown ZnO at the atomic scale remain an area of active investigation, as defects can significantly influence the material's electronic, optical, and mechanical properties.[15−17] The first part of the study is dedicated to the direct visualization of crystalline grains, grain boundaries, and atomic defects, including stacking faults and dipole disorder. By analyzing the spatial distribution and structure of these defects, we provide insights into the nucleation and growth mechanisms of ZnO films and their implications for functional properties.

The second part of the study examines the atomic-scale evolution of ZnO thin films under high-energy (200 keV)

Received: March 5, 2025
Revised: April 24, 2025
Accepted: April 25, 2025

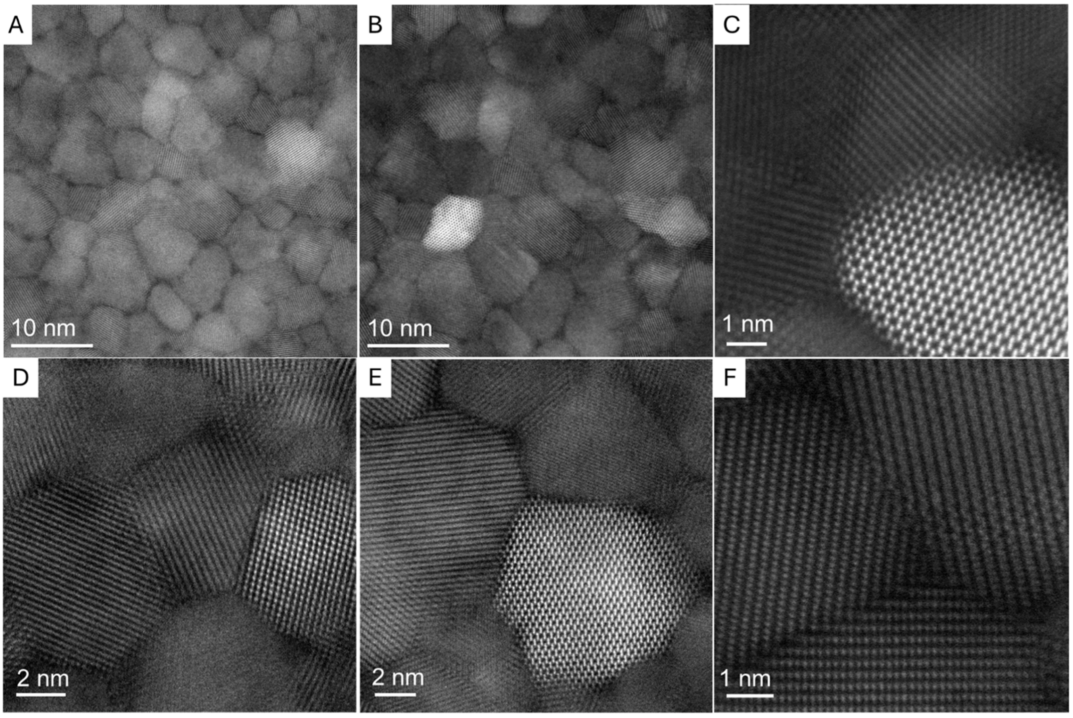

Figure 1. STEM imaging of ALD-grown ZnO thin film. (A) HAADF-STEM images of the grain texture observed in ZnO thin film. (B) LAADF-STEM image of the same region, where electron channeling effects are observed to brighten grains oriented along a low crystallographic zone axis. (C) LAADF STEM image of a grain oriented along the [001] direction where the honeycomb lattice is clearly resolved. Lattice fringes from neighboring grains are observed to be associated with the planes of the honeycomb lattice. (D) HAADF STEM image showing three grains at various twist grain boundaries. The grain furthest to the right is oriented along the [1−10] direction. (E) Similar boundary is observed between grains in a grain oriented along the [001] direction. (F) HAADF STEM image showing a triple point boundary composed of multiple high-angle twin grain boundaries.

electron bombardment through real-time STEM observations. While this electron energy falls within the lower range of electron radiation encountered in space environments such as the Van Allen belts (100 keV to 10 MeV),[18] the defects observed here serve as a foundational reference for future studies involving ex situ characterization of materials after high-energy (1−10 MeV) radiation. Importantly, the STEM results offer atomistic insights into the structural modifications induced by electron irradiation that help address long-standing scientific questions related to the atomic behavior of ZnO under electron irradiation. Together, our findings contribute to a deeper understanding of the mechanisms underlying the enhanced radiation resistance of ZnO, providing valuable insights for its application in space-grade microelectronics.

RESULTS

Using an aberration-corrected STEM, we investigated the nanostructure of the ALD-grown thin films. High-angle annular dark-field STEM (HAADF-STEM) images show that after 50 cycles of diethylzinc and water at 150 °C, the film is composed of packed crystalline grains. The nucleation density of the film was estimated to be near 31 ± 2 grains per 1000 nm^2 (n = 15) with an average crystal grain diameter of 6.8 ± 1.9 nm (Figure S1). Since the primary contrast mechanism in HAADF-STEM is mass−thickness, the intensity of the films suggests that film thickness is relatively uniform, as shown in Figure 1A. Atomic force microscopy of ZnO films on silicon substrates, grown under the same conditions as the TEM grids, confirms the films are uniform, with root mean squared roughness (RMS) measured below a nanometer (Figure S2). An identical location to Figure 1A is shown in the low-angle annular dark-field STEM (LAADF-STEM) image (Figure 1B), where variation in contrast along different crystalline domains is caused by differences in electron propagation through the sample, a process often referred to as electron channeling.[19] In practice, this results in grains observed near or along a low crystallographic zone axis producing more intense singles than grains mistitled from a crystallographic zone.[20] While this effect is present in both HAADF and LAADF imaging, the brightness difference is more prominent in LAADF and present under a larger range of tilt angles.[21] Leveraging this approach, crystals along a low zone axis—where atomic columns can be clearly distinguished—can be identified at relatively low magnifications and low electron dose rates (10−100 $e^-/Å^2$ s) without requiring significant beam exposure to determine their orientation.

As the following sections are focused on highlighting various atomic-scale defects observed in the ZnO films, a brief overview of the wurtzite ZnO structure is therefore included for context. The Wurtzite structure is described by the $P6_3mc$ space group, where the unit cell is composed of two pairs of Zn and O atoms. When viewed along the [100]-direction, the unit cell is composed of alternating Zn and O layers stacked along the [001]-direction. The relative positions of Zn and O atoms alternate relative to the (010) plane, giving rise to a characteristic alternating dipole moment (Figure S3). The structure is identical by symmetry when viewed along the b-direction, with the ZnO pairs also stacked in the [001]-direction but alternating dipoles along the [001]. As shown by the simulated HAADF-STEM image (Figure S4), the large

https://doi.org/10.1021/acsami.5c04571
ACS Appl. Mater. Interfaces XXXX, XXX, XXX−XXX

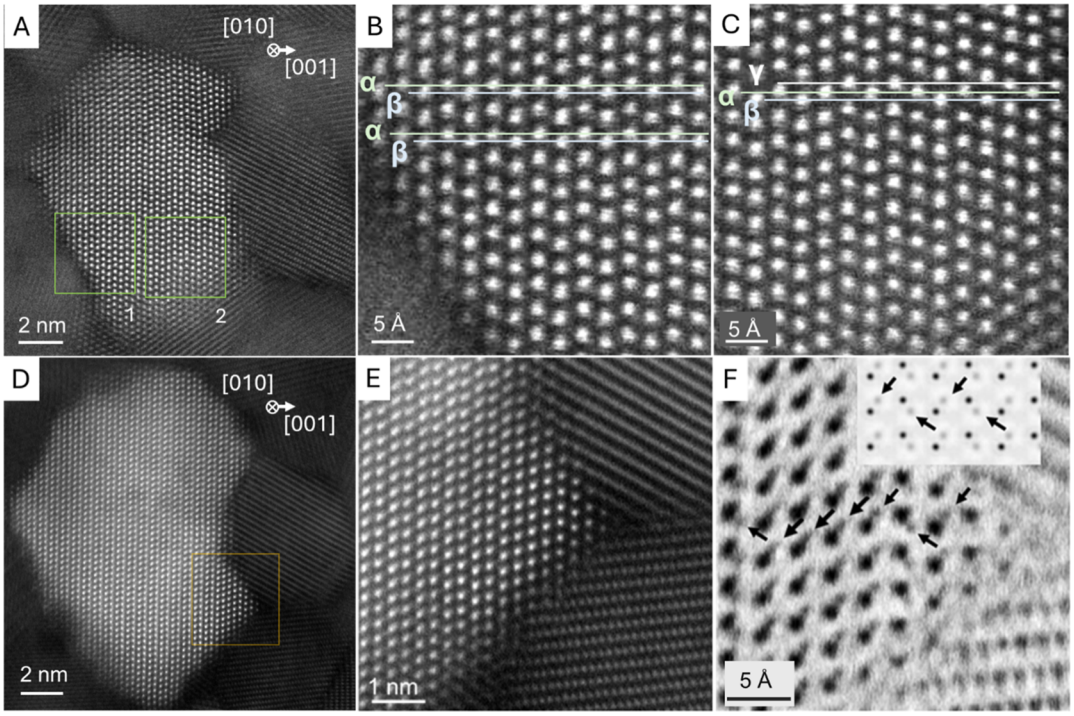

Figure 2. Intrinsic defects in ZnO thin film crystals. (A) HAADF STEM image of a defective wurtzite crystal oriented along the [010]-direction. Regions marked 1 and 2 are shown at a higher magnification in (B,C), respectively. The cation ordering in the pristine structure is described as alternating α, β planes, while the defective structures have a locally inserted plane with cations in the γ plane. (D) LAADF STEM image of grain with few structural defects, except for the marked enclosed region. A magnified view of this region (E) shows a stacking fault near a triple grain boundary. (F) BF STEM image resolving the position of oxygen columns shows the stacking fault is associated with a breaking of the dipole ordering. For comparison, inserted is a simulated BF STEM image with oxygen columns marked.

differences in the atomic number of Zn (Z = 30) and oxygen (Z = 8) make resolving the two simultaneously a challenge. Thus, in most crystals, we are limited to resolving the position columns composed of Zn atoms. This alone, however, as we show in this article, is enough to identify the presence of atomic defects. By convention, the [001] direction, as opposed to the [00−1] direction, is chosen to be the positive dipole moment (Zn-facing). Along this orientation, atomic columns contain alternating Zn and O atoms that are arranged to form a honeycomb lattice. As mentioned previously, while the [001] and [00−1] directions are not equivalent due to the direction of the ZnO dipole moment, in STEM, the two directions are not distinguishable since the 2D projections are equivalent.

The relatively small grain size present in the ZnO film allows for the atomic resolution imaging of various domains simultaneously—such as in Figure 1C−F. From these images, the coordination between grains can be determined. For example, Figure 1C shows a crystal oriented parallel to the [001] direction, as indicated by the clear hexagonal symmetry of the atomic lattice. Visible are two grains, directly to the left and above, from which lattice fringes are observable. In each, the visible lattice fringes correspond to spacings that can be determined from the honeycomb ZnO lattice; the domain to the left, composed of (010) planes and the top of (110) planes. This suggests that while the grains are misoriented with respect to one another, their orientations are not entirely random; instead, they appear to share a preferential alignment likely governed by a low-angle grain boundary or coincident lattice site. Such a relationship is not surprising given the high nucleation density and rapid coalescence of ZnO films under these conditions. It has been reported that on amorphous silica there is no crystallinity during the first ALD cycle of ZnO and that allows each subsequent layer to template the next layer.[22] As the film grows, these islands grow together and coalesce, and while perfect epitaxy is not enforced, energetic minimization favors certain low-angle boundaries or alignments between domains.

This can be probed directly, as STEM imaging allows for the direct observation of the nature of grain boundaries present in the film (Figure 1E,F). Most are twist grain boundaries (Figure 1D); however, high-angle twin grain boundaries are observed throughout, as shown in Figure 1F. While not the focus of this study, there is significant interest in quantifying grain boundary density due to its influence on the ferroelectric properties of ZnO;[23] STEM could be used to identify and quantify dopant segregations, as well as local changes in chemical bonding, at the interfaces in doped films.[24,25]

Throughout the ALD-grown ZnO thin film, we observed a variety of atomic defects in the bulk of the crystalline grains. A particle representative of this is shown in Figure 2A, from which two magnified regions, 1 and 2, are shown in Figure 2B,C respectively. The dark-field STEM images here are only able to resolve the Zn sublattice; however, these are sufficient to determine that the defects present throughout are stacking faults resulting from the addition (or removal) of one or multiple close-packed (cp) planes.[26] The insertion of cp planes can result in a variety of structures that are differentiated by the resulting position of Zn (denoted by Greek letters α, β, and γ) and oxygen (A, B, and C) along the c-axis. For example, Figure 2B shows a region with the expected wurtzite structure viewed along the [0−10] direction, where the alternating α, β, α, β, α, β, α, β, α, and β planes account for all the positions of the

https://doi.org/10.1021/acsami.5c04571
ACS Appl. Mater. Interfaces XXXX, XXX, XXX−XXX

atomic columns. In contrast, Figure 2C shows a highly defective region, where the atomic columns are described by the following: α, β, α, β, α, γ, α, γ, α, β, α, and β. This ordering corresponds to a type-I stacking fault, as described by Yan et al., which they calculated to be the most energetically favorable to form and are expected to introduce a downward shift in the conduction band minimum.[27]

From the crystal shown in the center of Figure 2D, we observe that these structural defects are also associated with disruptions to the dipole ordering of ZnO pairs. The core of the grain is largely free of structural defects; however, there is a region near the triple boundary toward the bottom right of the crystal where an extrinsic stacking fault (α, β, α, β, γ, β, and γ) is present (Figure 2E). A BF-STEM image in which the position of the oxygen atoms can be identified, Figure 2F, shows that at this defect, there is a clear breaking of dipole symmetry along the [001] direction. Contrary to the expected alternating dipole structure (projected along the [$\bar{1}$00] and [100]), the four defective columns are all oriented with a dipole projected along the [100]. The fact that an extrinsic stacking fault, which was calculated to have the highest formation energy,[27] is present suggests that a variety of stacking faults (Type I−III) should also be observed throughout. This result aligns with our frequent observations of highly defective crystals, often with defect types that are difficult to classify (Figure S5).

Stacking faults in the Zn sublattice can resemble another type of defect known as inversion boundaries. Inversion boundaries are a type of grain boundary where the wurtzite structure, viewed along the [010] direction, is inverted along the [001] plane. However, by resolving the positions of the oxygen columns, we confirm that no inversion boundaries are present. This is significant as inversion boundaries can create a 2D quantum well structure, which would influence the material's electronic properties.[28−31]

The growth of wurtzite ZnO through ALD is relatively common and has been reported thoroughly in the literature.[16,22] Several reviews have been dedicated to understanding the types of defects present, the most studied are native point defects—such as Zn and O vacancies as well as interstitials.[32,33] These are believed to strongly influence the materials' optical and electronic properties by changing the local Fermi levels, forming unstable atoms that can migrate, and acting as sinks for positive and negative charges.[34−37] In STEM, we are limited to observing 2D projections of 3D crystal structures. Point vacancies, unless present in very high concentrations, will be difficult to conclusively identify. The fact that the electron beam can also influence the sample structure, a topic discussed in detail in the following sections, would complicate further STEM studies related to the identification of point defects. Notably, none of the atomic-resolution STEM images showed the presence of Zn interstitial defects, which were computationally predicted.[32,38−40] Nonetheless, here, we unambiguously demonstrate that stacking faults are frequently observed in ZnO grains, offering a potential explanation for the radiation resistance of ZnO thin films. In cubic SiC, the presence of a high density of stacking faults has been attributed to an order of magnitude increase in radiation resistance.[41] Molecular dynamics simulations suggest this is due to the higher displacement energy required to displace atoms near stacking faults compared to those in the bulk lattice.[42]

Notably, since stacking faults are observed with greater frequency toward the [001] surface, these defects are likely associated with the distribution of oxygen vacancies during ALD crystal growth. Oxygen vacancies can locally disrupt the stoichiometry and symmetry of the growing lattice, especially in polar surfaces like [001], which can promote shear or slip necessary for stacking fault formation. Moreover, oxygen vacancies tend to cluster and migrate during film growth, potentially creating local strain fields that favor the nucleation of planar defects. Thus, the spatial distribution and dynamics of oxygen vacancies during deposition likely play a crucial role in guiding where and how extended defects such as stacking faults form. Understanding these defect structures is essential for tailoring the optical, electronic, and radiation-resistant properties of ZnO for future applications.

Direct Observation of Electron Beam Bombardment Effects in ZnO. Interestingly, beyond simply resisting radiation damage, ZnO has been shown to respond beneficially to high-energy electron bombardment, enhancing properties such as ultraviolet luminescence and hydrogen sensitivity in sensors.[12,14,43] In both cases, the formation of oxygen and zinc vacancies is proposed to explain the enhanced properties. Alternatively, some reports suggest that these radiation effects resemble changes observed in ZnO thin films after high-temperature annealing in a vacuum, such as an increase in crystal grain size.[13,44] As the vast majority of reported analysis relies on *post-mortem* bulk characterization, it is difficult to establish a clear understanding of the atomistic mechanisms underlying these changes. Here, based on in situ atomic resolution STEM observations, we find that the electron beam can significantly alter the atomic structure of ZnO crystalline grains, and we hypothesize that this offers insight into its enhanced properties after electron beam irradiation and, by extension, to the radiation resistance of ZnO.

STEM enables the use of a highly focused electron probe, reaching sub-Ångström dimensions (~70 pm), which can be precisely scanned over a fixed region, allowing for controlled irradiation of the sample. By measuring the electron probe current and defining the scan area, the number of electrons introduced into each region—referred to as fluence or dose (measured in $e^-/Å^2$)—can be quantified.

Electron beam damage in materials is broadly classified into two primary mechanisms: electron−atom interactions (knock-on damage/mass loss) and electron−electron interactions (radiolysis).[45] The first occurs when incoming electrons possess sufficient energy to surpass the ionization energy threshold, leading to inelastic collisions that displace atoms from their lattice positions. These displaced atoms can be sputtered on the material surface (forming a Frenkel-type defect) or are completely ejected from the sample, leading to mass loss.[46] In the present study, we operate the electron probe at a 200 kV accelerating voltage, which promotes the formation of holes and voids when the probe is held stationary for prolonged periods of time (Figure S6). This degradation indicates that incoming electrons possess enough energy to exceed the ionization energy threshold. We note that while such voids are largely absent during atomic resolution imaging, electron probe sample interactions will result in knock-on events that could lead to the formation of site vacancies, particularly in the zinc and oxygen sublattices, which have been shown to play a key role in the material's electronic and optical properties.[32,33,35,36] Since inelastic scattering events follow a Poisson distribution, the likelihood of knock-on damage

https://doi.org/10.1021/acsami.5c04571
ACS Appl. Mater. Interfaces XXXX, XXX, XXX−XXX

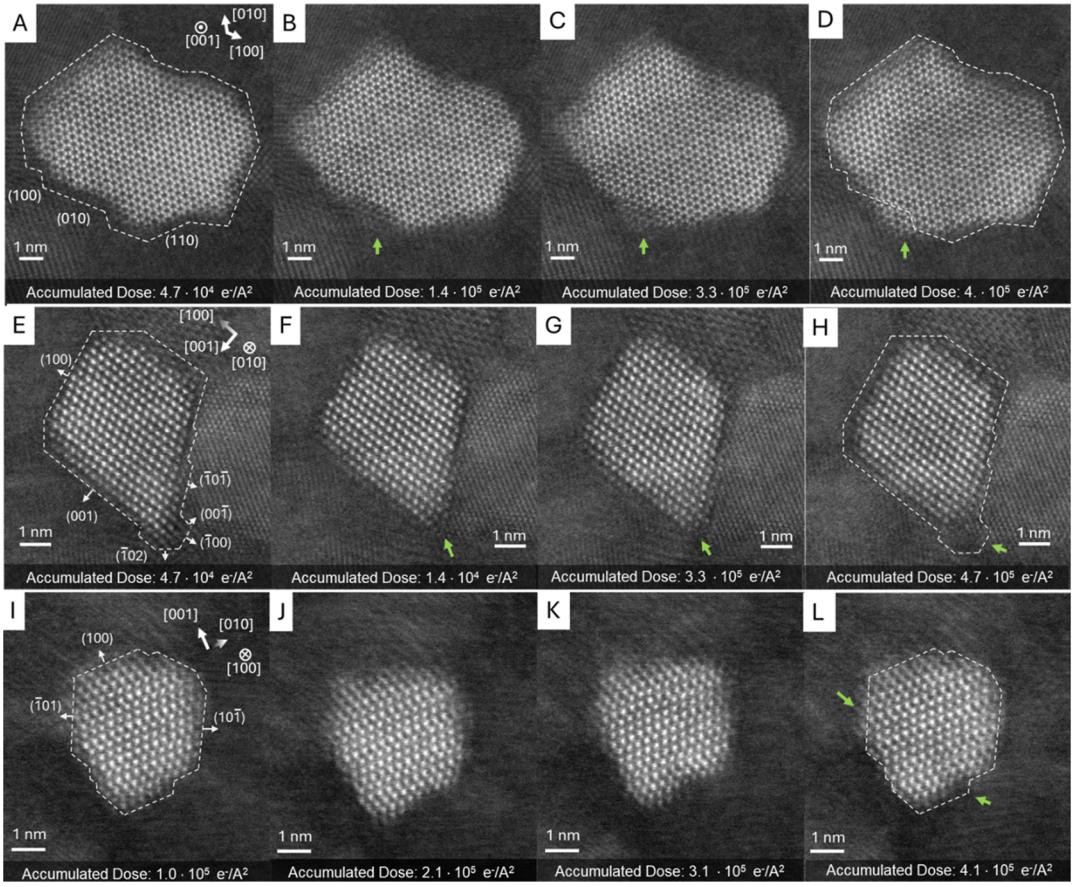

Figure 3. Evolution of ZnO crystalline grains under electron beam bombardment. Sequence 1 (A–D) shows a series of LAADF STEM images of a crystal along the [001] direction that is observed to undergo electron beam mediated growth. The estimated accumulated electron dosage is shown below each frame. (E–H) LAADF STEM images of a crystal oriented along the [010]-direction that is observed to decrease in size during electron beam exposure. (I–L) Under similar electron dose conditions, a third grain is observed not to undergo a significant transition.

increases with higher accumulated dose.[47] For this reason, special attention is placed on the accumulated dose at each step during imaging in a subsequent discussion.

The second form of beam-induced damage, radiolysis, occurs when high-energy electrons break chemical bonds and then generate free radicals. The effects of radiolysis are most prominent in samples with a significant amount of covalent bonds, such as organic compounds.[48−50] While the ionic Zn−O bonds are unlikely to be directly affected, the presence of trace water in the sample could lead to the formation of H^+ and OH^- species.[51] These reactive species then diffuse through the material, potentially altering its structure and properties. It has also been proposed that since water acts as a carrier recombination site in ZnO, water desorption driven by the electron probe may explain the enhanced ultraviolet emission observed in electron irradiated ZnO films.[12]

Similarly, there is emerging work suggesting that electrons can be used as coreactant during the ALD growth of materials.[52] This process—often referred to as electron-enhanced ALD—is enabled by the electron-stimulated desorption of surface ligands.[53,54] This process results in the production of chemically reactive sites that act as nucleation sites for crystal growth.

Real-time nanoscale observations of ZnO thin films under electron bombardment reveal a variety of behaviors. Figure 3 contains three sequences—four frames of each are shown—exhibiting the variety of beam-induced crystal effects. The first (Figure 3A–D) shows a crystalline grain oriented parallel to the [001] direction. The dashed line provides a visual of the crystal shape with primary crystal surface facets indicated in the image. The accumulated dosage is indicated below and is estimated to begin near 4.7×10^4 e^-/A^2 and is tracked until roughly ten times the initial dosage. During this electron beam exposure, a corner of the crystal is observed to grow in the bottom left, marked by a white arrow (Figure 3B,C). Overlaying the initial crystal shape with the final frame shows a clear difference in the crystal shape observed with the particle appearing to grow, particularly at the (010) surface termination. Notably, as opposed to forming Frenkel defects such as Zn interstitials,[32] the newly formed region maintains the honeycomb lattice symmetry, strongly suggesting the phenomena is not driven by knock-on damage.

Figure 3E–H shows a second transformation that occurs under similar electron dose conditions. The outlined particle is oriented along the [010] direction and is initially composed largely of (001) and (100) type facets. As electron beam exposure increases, the contrast from the atomic columns in the lower region of the crystal begins to fade and eventually disappears, as marked by the green arrow. Notably, during the electron beam exposure, the neighboring crystal to the right appears to grow into this region.

Not all crystals show clear signs of transformation under these electron dose conditions. For example, the crystal shown in Figure 3I–L shows very little discernible difference upon

https://doi.org/10.1021/acsami.5c04571
ACS Appl. Mater. Interfaces XXXX, XXX, XXX−XXX

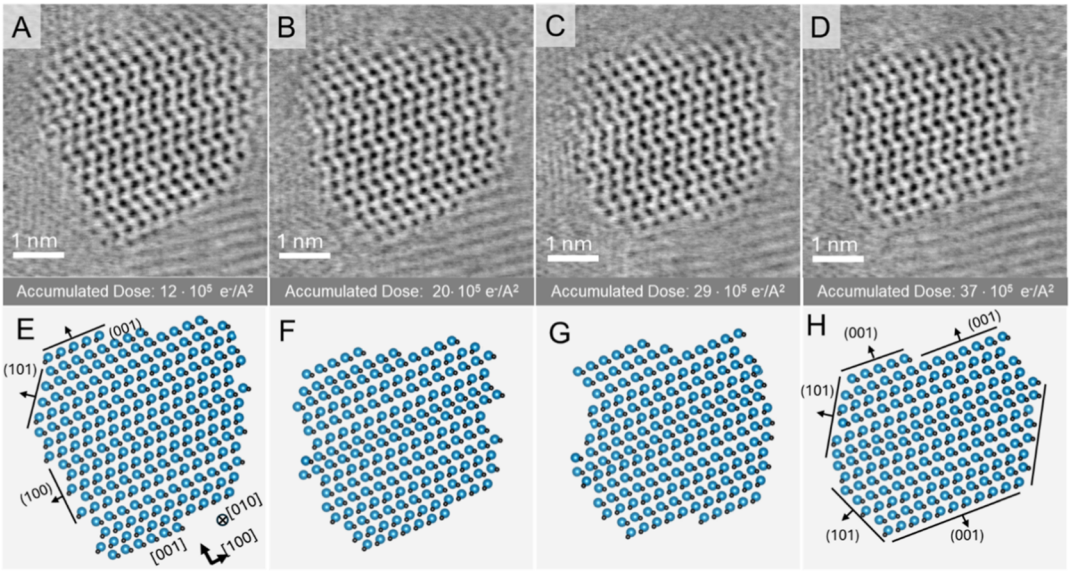

Figure 4. Surface reconstructions in ZnO grains exposed to harsh electron beam conditions. (A–D) BF-STEM images track a crystalline grain as it is in high electron dose conditions. The accumulated dose is ten times higher than previous sequences. (E–H) From each frame, an atomic model was constructed from which electron beam-induced changes to the crystal shape can be readily observed.

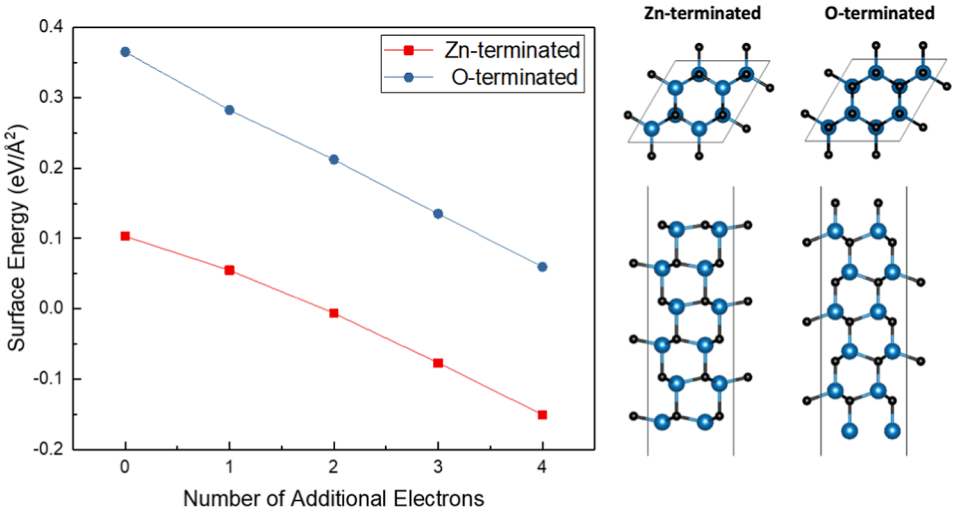

Figure 5. Surface energies of ZnO (001) slabs for Zn- and O-terminated surfaces under varying electron doping levels.

similar electron beam exposure. As shown in the BF-STEM images of the same grain during later imaging, electron beam-induced structural changes can be observed at significantly higher dose conditions (Figure 4A–D). A projected atomic model at each frame is shown in Figure 4E–H, from which we reach the following conclusions. First, the particle shape is observed to change significantly, reducing the amount of the (100)-type surface and instead forming with more (101) and (001) surfaces. Second, while both the (001) and (00−1) surfaces are observed to show some reconstruction, this reconstruction occurs asymmetrically with the oxygen facing the surface, which is observed to undergo a more significant reconstruction. This transformation is reminiscent of the observations by Look et al., who detected different types and degrees of defect formation upon electron irradiation in ZnO depending on whether it was Zn- or O-facing.[55]

The results here demonstrate that the interaction between the electron beam and ZnO extends beyond traditional electron beam damage observed in transition metal oxides.[46] This observation aligns with the existing literature suggesting that electron exposure can alter the properties of ZnO films.[12,14,43] However, comparisons across studies are challenging due to the wide range of electron accelerating voltages used. Some studies employ scanning electron microscopy operating at voltages below 30 kV, while others use much higher energy sources, reaching up to 10 MeV. At 200 kV, our findings fall between these extremes. The electron beam-induced crystal growth and surface reconstructions offer an explanation to the findings of Karuppasamy and Subrahmanyam, who observed more intense XRD peaks after electron bombardment.[13] This is consistent with our results showing that crystal *growth* occurs when the grain is parallel to the [001] direction. Notably, this crystal growth is surface-dependent, with particles oriented along the [010] (and [100]) direction either decreasing in size or undergoing surface reconstruction. This asymmetric growth during electron bombardment may be linked to the elongated structures observed by Siraj et al. in AFM studies of ZnO under high-

https://doi.org/10.1021/acsami.5c04571
ACS Appl. Mater. Interfaces XXXX, XXX, XXX−XXX

dose irradiation, though without additional structural characterization (e.g., XRD), this remains speculative.[44]

To evaluate the validity of this hypothesis, we compared the relative stabilities of Zn- vs O-terminated ZnO (001) surfaces, and to capture possible reconstructions under electron-rich conditions, we performed DFT calculations across a range of additional electron concentrations (Figure 5). The results show that both the Zn-terminated (001) and the O-terminated (001) slabs undergo a large reduction in surface energy with increasing electron dosage.

The calculated surface energies indicate that the O-terminated ZnO (001) surface consistently exhibits higher energy than the Zn-terminated surface across all electron doping levels. This suggests that the Zn-terminated surface is more thermodynamically stable under electron-rich conditions. Experimentally, the observed crystal reshaping under electron beam exposure shows a reduction in the number of (100)-type surfaces and an increase in the number of (101) and (001) facets. The calculated higher energy of the O-terminated (001) surface agrees with the experimental observation that surface reconstructions occur asymmetrically, with potentially more significant structural changes at O-terminated sites. This alignment between theory and experiment suggests that under electron-rich conditions the system favors Zn-terminated surfaces, driving the transformation of surface morphology to minimize overall surface energy.

Moreover, the crystal growth observed under electron beam exposure may help explain the enhanced radiation hardness of ZnO. The crystal growth that occurs upon electron beam exposure would increase the crystallinity of the film, and since the growth is observed to preserve the honeycomb lattice, it would reduce the presence of surface defects. Additionally, the reconstruction of the crystal shape leads to more energetically stable facet structure exposure upon electron beam bombardment.

CONCLUSIONS

In this study, we utilized aberration-corrected STEM to investigate the atomic structure of ALD-grown ZnO thin films, revealing atomic-scale insights into their morphologies, grain boundaries, and bulk defect structures. STEM imaging demonstrated that the films are composed of densely packed crystalline grains from which nucleation densities and grain orientations can be readily quantified. Atomic-resolution imaging allowed for the direct identification of stacking faults, including Type-I and extrinsic stacking faults, as well as dipole disorder within ZnO grains. These defects tend to be localized near the [001] surface, suggesting a strong correlation between structural imperfections and oxygen vacancy distributions during film growth. Notably, by controlling the oxygen environment during crystal growth, stacking fault formation can be selectively influenced, potentially enhancing the radiation resistance of the thin film.

A key novelty of this work is the direct observation of electron-beam-induced transformations, including localized crystal growth and structural reconstructions. We demonstrate that the electron beam exposure drives the crystal toward a more energetically stable surface structure, thus increasing the energy required to form radiation-induced localized defects. The observed electron-stimulated growth may also enhance the radiation hardness of ZnO by filling voids where charge accumulation could otherwise occur. Additionally, the observed asymmetry in surface reconstruction further highlights the role of Zn and O terminations in defect formation and stability. Our results suggest that ZnO thin films with exposed [00−1] facets exhibit greater radiation tolerance compared with those with the [001] facet exposed, a point that is important when designing thin films for semiconductor devices in extreme environments.

Overall, this study underscores the utility of advanced STEM techniques in characterizing the atomic-scale structure and dynamic behavior of ZnO thin films. The results provided atomic-scale insights into long-standing questions regarding the behavior of ZnO under electron irradiation and provide a foundation for further exploration of ZnO defect chemistry, its role in functional properties, and its potential applications in electronic and optoelectronic devices. Among these studies are those focused on understanding the differences in defects in films grown at higher temperatures or single crystal ZnO films, which would be expected to reduce the radiation resistance of the material.[56] Alternatively, the role of epitaxy, and as an extension, the atomic-scale structure of grain boundaries and density, remains relatively unexplored and could offer interesting insights. Importantly, the relatively small form factor combined with the precise control offered by ALD opens the door to a variety of future experiments where the response of the crystals to thermal annealing and biasing, in addition to electron transport measurements, can all be explored in situ within the STEM.

EXPERIMENTAL METHODS

Scanning Transmission Electron Microscopy. STEM analysis was conducted using a ThermoFisher Scientific Spectra 200 operated at an accelerating voltage of 200 kV. The probe semi-convergence angle was set to 15 mrad. Collection angles for HAADF and LAADF imaging were 72−200 and 17−65 mrad, respectively. Accumulated dosage and dose rates were estimated using the field of view, and the electron beam current was measured by the phosphorus screen and found to be typically between 70 and 80 pA.

STEM Simulations. Simulations were completed using Prismatic, which utilizes a plane-wave reciprocal-space interpolated scattering matrix to simulate STEM experiments.[57] The crystal structure of wurtzite ZnO was simulated from the CIF structure available in the Materials Project database: (mp-2133) from database version v2025.02.12.[58]

ALD Thin Film Growth. A Veeco Savannah 100 reactor was used to perform ALD of ZnO using diethylzinc and water vapor. TEM grids and witness Si samples were set directly on the heated chuck held at 150 °C during the deposition. ALD recipes were optimized previously (Figure S7), and the ALD recipe was 0.4−20−0.5−20 with N_2 carrier gas. The thickness of ZnO on the witness samples was confirmed after every deposition run. The STEM analysis reported in this paper was conducted on ALD-grown ZnO (50 cycles) on 3 mm copper TEM grids covered in amorphous silicon oxide film. The ZnO film thickness was approximately 9 nm.

Computational Details. Theoretical calculations were conducted using the Vienna Ab initio Simulation Program (VASP)[59−61] with the electron−ion interactions treated by the projector augmented wave (PAW) method. The exchange−correlation energy was approximated using the Perdew−Burke−Ernzerhof (PBE)[62,63] formulation within the generalized gradient approximation (GGA).[64,65] All calculations were carried out without spin polarization. van der Waals interactions were incorporated via the Grimme DFT-D3 method.[66] A cutoff energy of 500 eV was set, and the convergence thresholds were defined as 1×10^{-6} eV for total energy and 0.01 eV/Å for forces. The Brillouin zone integrations were performed with a 3 × 3 × 1 Monkhorst−Pack *k*-point mesh.[67]

Each ZnO (001) slab model consisted of 24 Zn and 24 O atoms, separated from its periodic images by a 10 Å vacuum region along the *z*-direction. The effect of adding a Hubbard *U* correction was assessed

https://doi.org/10.1021/acsami.5c04571
ACS Appl. Mater. Interfaces XXXX, XXX, XXX−XXX

following Dudarev's method,[68] using an effective U value of 5 eV for Zn d-states. This value is the same as used to obtain fitted elemental-phase reference energies by Stevanović et al.[69]

The surface energy E_{surf} is defined as

$$E_{surf} = (E_{slab} - E_{bulk})/2A$$

where E_{slab} and E_{bulk} are the energy of the slab and the energy of the selected surface, respectively. A is the in-plane area of the slab (the coefficient of 2 accounts for both sides of the slab).

■ ASSOCIATED CONTENT

Supporting Information

The Supporting Information is available free of charge at https://pubs.acs.org/doi/10.1021/acsami.5c04571.

Histogram of crystal size distribution; AFM image of ZnO film surface roughness; atomic models of wurtzite ZnO along low zone axis; simulated STEM images of wurtzite ZnO; LAADF STEM image of ZnO crystals with complex defects; evidence of knock-on damage at 200 kV; and ALD growth optimization (PDF)

■ AUTHOR INFORMATION

Corresponding Authors

Francisco Lagunas − *Applied Materials Division, Argonne National Laboratory, Lemont 60439 Illinois, United States;* orcid.org/0000-0002-6377-683X; Email: flagunasvargas@anl.gov

Jessica C. Jones − *Applied Materials Division, Argonne National Laboratory, Lemont 60439 Illinois, United States;* orcid.org/0000-0001-7475-4620; Email: jcjones@anl.gov

Authors

Shi Li − *Material Science Division, Argonne National Laboratory, Lemont 60439 Illinois, United States*

Zachary D. Hood − *Applied Materials Division, Argonne National Laboratory, Lemont 60439 Illinois, United States;* orcid.org/0000-0002-5720-4392

Complete contact information is available at: https://pubs.acs.org/10.1021/acsami.5c04571

Notes

The authors declare no competing financial interest.

■ ACKNOWLEDGMENTS

This material is based upon work supported by Laboratory Directed Research and Development (LDRD) funding from Argonne National Laboratory, provided by the Director, Office of Science, of the U.S. Department of Energy under Contract no. DE-AC02-06CH11357. Work performed at the Center for Nanoscale Materials, a U.S. Department of Energy Office of Science User Facility, was supported by the U.S. DOE, Office of Basic Energy Sciences, under Contract no. DE-AC02-06CH11357.

■ REFERENCES

(1) Özgür, U.·.; Alivov, Ya. I.; Liu, C.; Teke, A.; Reshchikov, M. A.; Doğan, S.; Avrutin, V.; Cho, S.-J.; Morkoç, H. A Comprehensive Review of ZnO Materials and Devices. *J. Appl. Phys.* **2005**, *98* (4), 041301.

(2) Kröger, F. A.; Meyer, H. J. G. The Edge Emission of ZnS, CdS and ZnO and Its Relation to the Lattice Vibrations of These Solids. *Physica* **1954**, *20* (7), 1149−1155.

(3) Dietz, R. E.; Hopfield, J. J.; Thomas, D. G. Excitons and the Absorption Edge of ZnO. *J. Appl. Phys.* **1961**, *32* (10), 2282−2286.

(4) Ramirez, J. I.; Li, Y. V.; Basantani, H.; Leedy, K.; Bayraktaroglu, B.; Jessen, G. H.; Jackson, T. N. Radiation-Hard ZnO Thin Film Transistors. *IEEE Trans. Nucl. Sci.* **2015**, *62* (3), 1399−1404.

(5) Vehse, W. E.; Sibley, W. A.; Keller, F. J.; Chen, Y. Radiation Damage in ZnO Single Crystals. *Phys. Rev.* **1968**, *167* (3), 828−836.

(6) Slater, J. C. The Effects of Radiation on Materials. *J. Appl. Phys.* **1951**, *22* (3), 237−256.

(7) Karnik, T.; Hazucha, P. Characterization of Soft Errors Caused by Single Event Upsets in CMOS Processes. *IEEE Trans. Dependable Secure Comput.* **2004**, *1* (2), 128−143.

(8) Lorenz, K.; Peres, M.; Franco, N.; Marques, J. G.; Miranda, S. M. C.; Magalhães, S.; Monteiro, T.; Wesch, W.; Alves, E.; Wendler, E. Radiation Damage Formation and Annealing in GaN and ZnO. In *Oxide-based Materials and Devices II*; SPIE, 2011; Vol. *7940*, pp 135−148.

(9) Rasmidi, R.; Duinong, M.; Chee, F. P. Radiation Damage Effects on Zinc Oxide (ZnO) Based Semiconductor Devices− a Review. *Radiat. Phys. Chem.* **2021**, *184*, 109455.

(10) Zhao, D.; Mourey, D. A.; Jackson, T. N. Gamma-Ray Irradiation of ZnO Thin Film Transistors and Circuits. *68th Device Research Conference*, 2010; pp 241−242.

(11) Tuomisto, F.; Saarinen, K.; Look, D. C.; Farlow, G. C. Introduction and Recovery of Point Defects in Electron-Irradiated ZnO. *Phys. Rev. B: Condens. Matter Mater. Phys.* **2005**, *72* (8), 085206.

(12) Xie, R.; Sekiguchi, T.; Ishigaki, T.; Ohashi, N.; Li, D.; Yang, D.; Liu, B.; Bando, Y. Enhancement and Patterning of Ultraviolet Emission in ZnO with an Electron Beam. *Appl. Phys. Lett.* **2006**, *88* (13), 134103.

(13) Karuppasamy, A.; Subrahmanyam, A. Effect of Electron Bombardment on the Properties of ZnO Thin Films. *Mater. Lett.* **2007**, *61* (4), 1256−1259.

(14) Kim, J.-H.; Mirzaei, A.; Woo Kim, H.; Wu, P.; Kim, S. S. Design of Supersensitive and Selective ZnO-Nanofiber-Based Sensors for H2 Gas Sensing by Electron-Beam Irradiation. *Sens. Actuators, B* **2019**, *293*, 210−223.

(15) Mishra, S.; Przezdziecka, E.; Wozniak, W.; Adhikari, A.; Jakiela, R.; Paszkowicz, W.; Sulich, A.; Ozga, M.; Kopalko, K.; Guziewicz, E. Structural Properties of Thin ZnO Films Deposited by ALD under O-Rich and Zn-Rich Growth Conditions and Their Relationship with Electrical Parameters. *Materials* **2021**, *14* (14), 4048.

(16) Bielinski, A. R.; Kazyak, E.; Schlepütz, C. M.; Jung, H. J.; Wood, K. N.; Dasgupta, N. P. Hierarchical ZnO Nanowire Growth with Tunable Orientations on Versatile Substrates Using Atomic Layer Deposition Seeding. *Chem. Mater.* **2015**, *27* (13), 4799−4807.

(17) Martinson, A. B. F.; Elam, J. W.; Hupp, J. T.; Pellin, M. J. ZnO Nanotube Based Dye-Sensitized Solar Cells. *Nano Lett.* **2007**, *7* (8), 2183−2187.

(18) Vogl, T.; Sripathy, K.; Sharma, A.; Reddy, P.; Sullivan, J.; Machacek, J. R.; Zhang, L.; Karouta, F.; Buchler, B. C.; Doherty, M. W.; Lu, Y.; Lam, P. K. Radiation Tolerance of Two-Dimensional Material-Based Devices for Space Applications. *Nat. Commun.* **2019**, *10* (1), 1202.

(19) Howie, A. Diffraction Channelling of Fast Electrons and Positrons in Crystals. *Philos. Mag. J. Theor. Exp. Appl. Phys.* **1966**, *14* (128), 223−237.

(20) Kourkoutis, L. F.; Parker, M. K.; Vaithyanathan, V.; Schlom, D. G.; Muller, D. A. Direct Measurement of Electron Channeling in a Crystal Using Scanning Transmission Electron Microscopy. *Phys. Rev. B: Condens. Matter Mater. Phys.* **2011**, *84* (7), 075485.

(21) Yu, Z.; Muller, D. A.; Silcox, J. Effects of Specimen Tilt in ADF-STEM Imaging of a-Si/c-Si Interfaces. *Ultramicroscopy* **2008**, *108* (5), 494−501.

(22) Boichot, R.; Tian, L.; Richard, M.-I.; Crisci, A.; Chaker, A.; Cantelli, V.; Coindeau, S.; Lay, S.; Ouled, T.; Guichet, C.; Chu, M. H.; Aubert, N.; Ciatto, G.; Blanquet, E.; Thomas, O.; Deschanvres, J.-L.; Fong, D. D.; Renevier, H. Evolution of Crystal Structure During

the Initial Stages of ZnO Atomic Layer Deposition. *Chem. Mater.* **2016**, *28* (2), 592−600.
(23) Straumal, B. B.; Protasova, S. G.; Mazilkin, A. A.; Goering, E.; Schütz, G.; Straumal, P. B.; Baretzky, B. Ferromagnetic Behaviour of ZnO: The Role of Grain Boundaries. *Beilstein J. Nanotechnol.* **2016**, *7*, 1936−1947.
(24) Lagunas, F.; Alexander, G.; Lee Punaro, A.; Moscosa, C.; Hu, L.; Cabana, J.; Klie, R. F. Structural Transformations at the Atomic Scale in Spinel Vanadium Oxides upon Mg2+ Extraction. *ACS Appl. Energy Mater.* **2023**, *6* (11), 5681−5689.
(25) Futazuka, T.; Ishikawa, R.; Shibata, N.; Ikuhara, Y. Grain Boundary Structural Transformation Induced by Co-Segregation of Aliovalent Dopants. *Nat. Commun.* **2022**, *13* (1), 5299.
(26) Stampfl, C.; Van de Walle, C. G. Energetics and Electronic Structure of Stacking Faults in AlN, GaN, and InN. *Phys. Rev. B: Condens. Matter Mater. Phys.* **1998**, *57* (24), R15052−R15055.
(27) Yan, Y.; Dalpian, G. M.; Al-Jassim, M. M.; Wei, S.-H. Energetics and Electronic Structure of Stacking Faults in ZnO. *Phys. Rev. B: Condens. Matter Mater. Phys.* **2004**, *70* (19), 193206.
(28) Ribić, V.; Rečnik, A.; Komelj, M.; Kokalj, A.; Branković, Z.; Zlatović, M.; Branković, G. New Inversion Boundary Structure in Sb-Doped ZnO Predicted by DFT Calculations and Confirmed by Experimental HRTEM. *Acta Mater.* **2020**, *199*, 633−648.
(29) Kim, J. C.; Goo, E. Inversion Twin Boundaries in Zinc Oxide. *J. Am. Ceram. Soc.* **1990**, *73* (4), 877−884.
(30) Li, S.; Lei, H.; Wang, Z.; Chen, J.; Ruterana, P. Energetic and Electronic Properties of (0001) Inversion Domain Boundaries in ZnO. *Phys. Status Solidi B* **2018**, *255* (4), 1700429.
(31) Liu, Y. Z.; Yuan, H. T.; Zeng, Z. Q.; Du, X. L.; Han, X. D.; Xue, Q. K.; Zhang, Z. Inversion Domain Boundary in a ZnO Film. *Philos. Mag. Lett.* **2007**, *87* (9), 687−693.
(32) Janotti, A.; Van de Walle, C. G. Native Point Defects in ZnO. *Phys. Rev. B: Condens. Matter Mater. Phys.* **2007**, *76* (16), 165202.
(33) Gurylev, V.; Perng, T. P. Defect Engineering of ZnO: Review on Oxygen and Zinc Vacancies. *J. Eur. Ceram. Soc.* **2021**, *41* (10), 4977−4996.
(34) Liao, Z.-M.; Zhang, H.-Z.; Zhou, Y.-B.; Xu, J.; Zhang, J.-M.; Yu, D.-P. Surface Effects on Photoluminescence of Single ZnO Nanowires. *Phys. Lett. A* **2008**, *372* (24), 4505−4509.
(35) Ansari, S. A.; Khan, M. M.; Kalathil, S.; Nisar, A.; Lee, J.; Cho, M. H. Oxygen Vacancy Induced Band Gap Narrowing of ZnO Nanostructures by an Electrochemically Active Biofilm. *Nanoscale* **2013**, *5* (19), 9238−9246.
(36) Kohan, A. F.; Ceder, G.; Morgan, D.; Van de Walle, C. G. First-Principles Study of Native Point Defects in ZnO. *Phys. Rev. B: Condens. Matter Mater. Phys.* **2000**, *61* (22), 15019−15027.
(37) Li, X.; Song, J.; Liu, Y.; Zeng, H. Controlling Oxygen Vacancies and Properties of ZnO. *Curr. Appl. Phys.* **2014**, *14* (3), 521−527.
(38) Sun, Y.; Wang, H. The Electronic Properties of Native Interstitials in ZnO. *Phys. B* **2003**, *325*, 157−163.
(39) Oba, F.; Choi, M.; Togo, A.; Tanaka, I. Point Defects in ZnO: An Approach from First Principles. *Sci. Technol. Adv. Mater.* **2011**, *12* (3), 034302.
(40) Janotti, A.; Van de Walle, C. G. New Insights into the Role of Native Point Defects in ZnO. *J. Cryst. Growth* **2006**, *287* (1), 58−65.
(41) Zhang, Y.; Ishimaru, M.; Varga, T.; Oda, T.; Hardiman, C.; Xue, H.; Katoh, Y.; Shannon, S.; Weber, W. J. Nanoscale Engineering of Radiation Tolerant Silicon Carbide. *Phys. Chem. Chem. Phys.* **2012**, *14* (38), 13429−13436.
(42) Jiang, M.; Peng, S. M.; Zhang, H. B.; Xu, C. H.; Xiao, H. Y.; Zhao, F. A.; Liu, Z. J.; Zu, X. T. Ab Initio Molecular Dynamics Simulation of the Effects of Stacking Faults on the Radiation Response of 3C-SiC. *Sci. Rep.* **2016**, *6* (1), 20669.
(43) Hui, K. C.; An, J.; Zhang, X. Y.; Xu, J. B.; Dai, J. Y.; Ong, H. C. Electron Beam Induced Light Emission and Charge Conduction Patterning in ZnO by Using an AlO Layer. *Adv. Mater.* **2005**, *17* (16), 1960−1964.
(44) Siraj, K.; Kanwal, M.; Saleem, S.; Pedarnig, J. D.; Rafique, M. S.; Naseem, S. Electron Beam Fracturing of ZnO Nanostructures and Modification in Optical Band Gap. *Indian J. Phys.* **2016**, *90* (12), 1431−1436.
(45) Egerton, R. F.; Li, P.; Malac, M. Radiation Damage in the TEM and SEM. *Micron* **2004**, *35* (6), 399−409.
(46) Jiang, N. Electron Beam Damage in Oxides: A Review. *Rep. Prog. Phys.* **2016**, *79* (1), 016501.
(47) Peters, J. J. P.; Reed, B. W.; Jimbo, Y.; Noguchi, K.; Müller, K. H.; Porter, A.; Masiel, D. J.; Jones, L. Event-Responsive Scanning Transmission Electron Microscopy. *Science* **2024**, *385* (6708), 549−553.
(48) Lagunas, F.; Bugallo, D.; Karimi, F.; Yang, Y.; Badr, H. O.; Cope, J. H.; Ferral, E.; Barsoum, M. W.; Hu, Y.-J.; Klie, R. F. Ion-Exchange Effects in One-Dimensional Lepidocrocite TiO2: A Cryogenic Scanning Transmission Electron Microscopy and Density Functional Theory Study. *Chem. Mater.* **2024**, *36* (6), 2743−2755.
(49) Zhou, C.; Wang, D.; Lagunas, F.; Atterberry, B.; Lei, M.; Hu, H.; Zhou, Z.; Filatov, A. S.; Jiang, D.; Rossini, A. J.; Klie, R. F.; Talapin, D. V. Hybrid Organic−Inorganic Two-Dimensional Metal Carbide MXenes with Amido- and Imido-Terminated Surfaces. *Nat. Chem.* **2023**, *15*, 1722−1729.
(50) Lagunas, F.; Zhou, C.; Wang, D.; Thakur, A.; Anasori, B.; Talapin, D. V.; Hood, Z. D.; Klie, R. F. In Situ Formation of Ripplocations in Hybrid Organic−Inorganic MXenes. *Adv. Mater.* **2025**, *37* (13), 2411669.
(51) Fritsch, B.; Lee, S.; Körner, A.; Schneider, N. M.; Ross, F. M.; Hutzler, A. The Influence of Ionizing Radiation on Quantification for In Situ and Operando Liquid-Phase Electron Microscopy. *Adv. Mater.* **2025**, *37* (13), 2415728.
(52) Collings, M. A.; Junige, M.; Cavanagh, A. S.; Wang, V.; Kummel, A. C.; George, S. M. Electron-Enhanced Atomic Layer Deposition of Ru Thin Films Using Ru(DMBD)(CO)3 and Effect of Forming Gas Anneal. *J. Vac. Sci. Technol., A* **2023**, *41* (6), 062408.
(53) van Dorp, W. F.; Hansen, T. W.; Wagner, J. B.; De Hosson, J. T. M. The Role of Electron-Stimulated Desorption in Focused Electron Beam Induced Deposition. *Beilstein J. Nanotechnol.* **2013**, *4* (1), 474−480.
(54) Sprenger, J. K.; Sun, H.; Cavanagh, A. S.; Roshko, A.; Blanchard, P. T.; George, S. M. Electron-Enhanced Atomic Layer Deposition of Boron Nitride Thin Films at Room Temperature and 100 °C. *J. Phys. Chem. C* **2018**, *122* (17), 9455−9464.
(55) Look, D. C.; Reynolds, D. C.; Hemsky, J. W.; Jones, R. L.; Sizelove, J. R. Production and Annealing of Electron Irradiation Damage in ZnO. *Appl. Phys. Lett.* **1999**, *75* (6), 811−813.
(56) Jamison, L.; Zheng, M.-J.; Shannon, S.; Allen, T.; Morgan, D.; Szlufarska, I. Experimental and Ab Initio Study of Enhanced Resistance to Amorphization of Nanocrystalline Silicon Carbide under Electron Irradiation. *J. Nucl. Mater.* **2014**, *445* (1), 181−189.
(57) Rangel DaCosta, L.; Brown, H. G.; Pelz, P. M.; Rakowski, A.; Barber, N.; O'Donovan, P.; McBean, P.; Jones, L.; Ciston, J.; Scott, M. C.; Ophus, C. Prismatic 2.0 − Simulation Software for Scanning and High Resolution Transmission Electron Microscopy (STEM and HRTEM). *Micron* **2021**, *151*, 103141.
(58) Jain, A.; Ong, S. P.; Hautier, G.; Chen, W.; Richards, W. D.; Dacek, S.; Cholia, S.; Gunter, D.; Skinner, D.; Ceder, G.; Persson, K. A. Commentary: The Materials Project: A Materials Genome Approach to Accelerating Materials Innovation. *APL Mater.* **2013**, *1* (1), 011002.
(59) Kresse, G.; Furthmüller, J. Efficiency of Ab-Initio Total Energy Calculations for Metals and Semiconductors Using a Plane-Wave Basis Set. *Comput. Mater. Sci.* **1996**, *6* (1), 15−50.
(60) Kresse, G.; Hafner, J. Ab Initio Molecular-Dynamics Simulation of the Liquid-Metal–Amorphous-Semiconductor Transition in Germanium. *Phys. Rev. B: Condens. Matter Mater. Phys.* **1994**, *49* (20), 14251−14269.
(61) Kresse, G.; Furthmüller, J. Efficient Iterative Schemes for Ab Initio Total-Energy Calculations Using a Plane-Wave Basis Set. *Phys. Rev. B: Condens. Matter Mater. Phys.* **1996**, *54* (16), 11169−11186.
(62) Blöchl, P. E. Projector Augmented-Wave Method. *Phys. Rev. B: Condens. Matter Mater. Phys.* **1994**, *50* (24), 17953−17979.

https://doi.org/10.1021/acsami.5c04571
ACS Appl. Mater. Interfaces XXXX, XXX, XXX−XXX

(63) Hohenberg, P.; Kohn, W. Inhomogeneous Electron Gas. *Phys. Rev.* **1964**, *136* (3B), B864−B871.
(64) Perdew, J. P.; Burke, K.; Ernzerhof, M. Generalized Gradient Approximation Made Simple. *Phys. Rev. Lett.* **1996**, *77* (18), 3865−3868.
(65) Perdew, J. P.; Yue, W. Accurate and Simple Density Functional for the Electronic Exchange Energy: Generalized Gradient Approximation. *Phys. Rev. B: Condens. Matter Mater. Phys.* **1986**, *33* (12), 8800−8802.
(66) Grimme, S.; Antony, J.; Ehrlich, S.; Krieg, H. A Consistent and Accurate Ab Initio Parametrization of Density Functional Dispersion Correction (DFT-D) for the 94 Elements H-Pu. *J. Chem. Phys.* **2010**, *132* (15), 154104.
(67) Monkhorst, H. J.; Pack, J. D. Special Points for Brillouin-Zone Integrations. *Phys. Rev. B: Solid State* **1976**, *13* (12), 5188−5192.
(68) Dudarev, S. L.; Botton, G. A.; Savrasov, S. Y.; Humphreys, C. J.; Sutton, A. P. Electron-Energy-Loss Spectra and the Structural Stability of Nickel Oxide: An LSDA+U Study. *Phys. Rev. B: Condens. Matter Mater. Phys.* **1998**, *57* (3), 1505−1509.
(69) Stevanović, V.; Lany, S.; Zhang, X.; Zunger, A. Correcting Density Functional Theory for Accurate Predictions of Compound Enthalpies of Formation: Fitted Elemental-Phase Reference Energies. *Phys. Rev. B: Condens. Matter Mater. Phys.* **2012**, *85* (11), 115104.

https://doi.org/10.1021/acsami.5c04571
ACS Appl. Mater. Interfaces XXXX, XXX, XXX−XXX